Journal of Marine Science and Application (2026) 25: 1160-1175
https://doi.org/10.1007/s11804-025-00715-3

RESEARCH ARTICLE

Performance Comparison and the Influence of Cross-sectional Shape in Piezoelectric Energy Harvester Using Vortex-induced and Wake-induced Vibration

Muhao Wang[1], Yanchang Sun[1], Dongjian Zhao[1], Xiaoya Zhang[1], Derong Duan[1], Hui Zhang[1] and Changqing Gao[1]

Received: 18 April 2025 / Accepted: 22 August 2025
© Harbin Engineering University and Springer-Verlag GmbH Germany, part of Springer Nature 2026

Abstract

To demonstrate the superiority of wake-induced vibration (WIV) in flow-induced vibration piezoelectric energy harvesting, a novel integrated dual-bluff-body piezoelectric energy harvester (PEH) was proposed in this paper. Wind tunnel experiments were conducted to investigate the impact of different cross-sectional shapes on the output performance of the device. The operational mechanism was analyzed using two-way fluid–structure interaction theory. Results show that the integrated structural design not only significantly improved the output performance of the PEH but also facilitated device miniaturization, overcoming the limitations of complex structures and challenges in miniaturization in existing technologies. Compared to vortex-induced vibration, the PEH driven by WIV achieved a 177.2% increase in maximum output voltage and a 66.7% expansion in effective operational range. Among the tested cross-sectional shapes, a circular interference column delivered the best performance under WIV, with maximum output power exceeding that of square and equilateral triangular cross-sections by 60.65% and 44.4%, respectively. Moreover, the second peak in energy conversion efficiency associated with the circular cross-section exhibited a coverage area 2.4 times larger than that of a square cross-section, enabling stable energy output across a broad range of wind speeds. These findings offer important insights into the application of FIV in piezoelectric energy harvesting and provide strong support for the advancement of self-powered technology.

Keywords Piezoelectric energy harvester; Output performance; Wake-induced vibration; Energy conversion efficiency; Effective operational range

1 Introduction

In the field of nearshore sea surface monitoring, the rapid development of wireless sensor technologies has substantially increased the energy consumption of microelectronic components, highlighting the urgent need for self-powered technologies (Zuo et al., 2020). Among various approaches, flow-induced vibration (FIV) energy harvesting has attracted considerable attention due to its self-excitation and high sensitivity to microfluidic environments. This technology has demonstrated excellent energy-harvesting performance and broad application prospects in micro-scale devices (Latif et al., 2023).

FIV technology encompasses various vibration mechanisms, such as vortex-induced vibration (VIV), galloping, flutter, and wake-induced vibration (WIV). Leveraging these mechanisms, researchers have developed numerous flow-induced vibration piezoelectric energy harvesters (FIVPEHs) to improve the energy-harvesting efficiency of such devices. For example, by optimizing the effects of VIV, Wang et al. (2021) achieved a 15.6% increase in vibration amplitude and a 31.3% improvement in displacement in their experimental setup. Wang et al. (2023a) successfully transformed the vibration mechanism of their device from VIV to galloping, resulting in a substantially broader operating bandwidth and an increase in output power of up to 471.2%. Similarly, Eugeni et al. (2020) conducted flutter experiments by placing a cantilevered flag in a subsonic wind tunnel, achieving a maximum output power of 1.12 mW from their test prototype. In another study, Farsi

Article Highlights

- An integrated double-bluff body piezoelectric energy harvester is proposed.
- Performance under wake-induced vibration and vortex-induced vibration is compared.
- Effects of arrangement and fluid velocity on characteristics are revealed.
- Energy-harvesting mechanism by wake-induced vibration is revealed.

✉ Derong Duan
me_duandr@ujn.edu.cn

[1] School of Mechanical Engineering, University of Jinan, Jinan 250022, China

et al. (2021) reported a 66% increase in vibration amplitude under WIV, resulting in a 300% improvement in output power. To further enhance the performance of piezoelectric energy harvesters (PEHs), numerous researchers have investigated various approaches across different vibration mechanisms (Wang et al., 2020a). These approaches include constructing multi-degree-of-freedom systems (Franzini and Bunzel, 2018), introducing nonlinear electromagnetic forces (Zhang et al., 2017), and optimizing the surface structures of bluff bodies (Hu et al., 2019).

Modifying the shape of the bluff body is a proven and effective approach to optimizing the performance of FIVPEHs. Changing the cross-sectional shape of the bluff body can substantially alter the dynamic behavior of the system (Yang et al., 2020). In a previous study, Abdelkefi et al. (2012) compared the output power of square, D-shaped, and triangular cross-sectional bluff bodies. They found that a triangular cross-section with a top angle of 30° performed better at low flow rates, whereas the D-shaped cross-sectional bluff body yielded superior performance at high flow rates. Additionally, Zhu et al. (2021) examined the effects of a trapezoidal bluff body cross-section on the energy-harvesting characteristics of the device. The output performance of the device was found to substantially vary under different flow field interferences. Wang et al. (2019) examined isosceles triangular bluff bodies with varying apex angles and found that obtuse-angled triangles are beneficial for galloping-based energy harvesting. Wang et al. (2020b) introduced novel PEHs featuring spindle and butterfly-shaped bluff bodies. Flow field analysis revealed that these PEHs exhibited VIV at low wind speeds and transitioned to galloping at high wind speeds. Notably, the spindle-shaped cross-sectional bluff body with a narrow width ratio reduced the threshold wind speed by over 13% and increased the maximum voltage output by more than 160%. Overall, these findings highlight that the energy-harvesting performance is highly sensitive to different shapes of bluff bodies. Specifically, the cross-sectional shape plays a crucial role in the energy-harvesting performance of the device (Wang et al., 2020c).

Compared to enhancing the energy-harvesting characteristics of the device by altering the aerodynamic performance of a single bluff body, the introduction of a double-bluff body model also leads to a notable improvement in energy-harvesting efficiency. For example, Zhao et al. (2021) investigated the energy harvesting of a wake-induced vibration piezoelectric energy harvester (WIVPEH) with a double-bluff body configuration, using inverted D-shaped, circular, and D-shaped cylinders as upstream interference columns. They found that the power densities of the three configurations were 43.2, 25.3, and 31 times higher than those without wake interference, respectively. The energy-harvesting performance of the WIVPEH with double bluff bodies was markedly superior to that of the VIV and galloping PEH without wake interference. Similarly, Zhang and Wang (2016) found that for the same energy-harvesting device, WIV resulted in higher maximum power output and better energy-harvesting characteristics compared to VIV. However, their study was limited to evaluating energy-harvesting performance with a specific upstream interference column shape. Wang et al. (2022) demonstrated through flow field analysis that the performance of a tandem bluff body system was influenced by the shape of the upstream bluff body on the waterward side. Their results showed that the output power of the PEH driven by WIV in a double-column flow was 111% higher than that of a single-column PEH. However, their device used a split arrangement that hindered miniaturization, making it unsuitable for powering micro-sensors.

Overall, the vibration mode of the PEH and the aerodynamic shape of the bluff body play a crucial role in determining the output performance of the device. While existing studies have extensively explored PEHs, research on energy harvesting using WIV is lacking, with most existing work focusing on split-type layouts. These designs often suffer from complex structures and challenges related to miniaturization. Aiming to address these limitations, this study proposed an integrated double-bluff body PEH based on WIV. By adjusting the device structure, the cantilever load could be adjusted, effectively improving the output performance of the PEH and expanding its effective operating range. Additionally, the design simplified the structural size and the installation method, making it highly conducive to device miniaturization. A WIV energy harvesting experimental platform was developed to assess the vibration response and output performance of the PEH under different WIV configurations, using two-way fluid–structure interaction (FSI) theory for analysis. This study revealed the response mechanism of the PEH under VIV and WIV conditions and clarified the influence of the cross-sectional shape of the interference column on the output performance of the PEH under WIV. The findings of this study contribute to the development of highly efficient energy-harvesting system configurations that can meet the self-powering demands of micro-sensors in the information age, offering valuable insights for the design of future FIVPEHs.

2 Methods and experiments

2.1 Experimental Installation

A wind tunnel test bench was constructed to investigate the energy-harvesting performance of the integrated double-bluff body PEH based on WIV, as shown in Figure 1.

The principal diagram of the wind tunnel experiment, conducted in air, is shown in Figure 1(a). An axial-flow

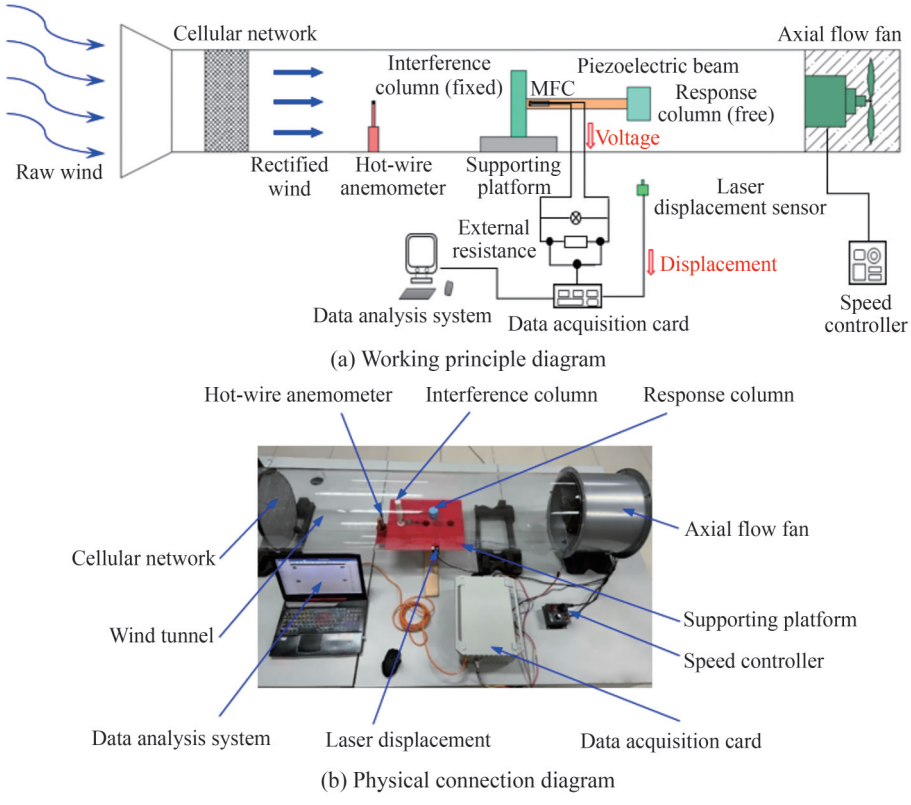


Figure 1 Working principle and physical connection diagram of the WIVPEH

fan draws air from the left end of the tunnel, with wind speed regulated by adjusting the fan speed. The external airflow is then rectified using a honeycomb network to form a stable flow field. Upon reaching the bluff body model in the middle of the wind tunnel, the flow generates a corresponding excitation. This excitation causes the deformation of the piezoelectric oscillator model, which, in turn, generates electrical signals that are transmitted to an external circuit. A hot-wire anemometer is used to measure the wind speed of the incoming flow, while a laser displacement sensor (GC05-200NW) records the vibration signal of the response column. The data acquisition card (DH5922D) collects the electrical and vibration signals generated by the PEH.

Aiming to facilitate a clear comparison of the power generation performance across different PEH configurations, the influence of complex post-processing circuits was excluded. Instead, an external circuit comprising a light-emitting diode (LED) in parallel with a pure resistor was adopted. The resistor was set to 1 MΩ, a value that provided near-maximum power output across all tested wind speeds and closely matched the measured internal impedance of the PEH. This setup ensured reliable and consistent comparative results. Based on this principle, a wind tunnel test bench was constructed to evaluate the performance of the PEHs, as shown in Figure 1(b). Following the experiment, the time- and frequency-domain responses of the PEH were analyzed and calculated using a data analysis system (DHDAS). Aiming to ensure accuracy, each data point was averaged over three separate measurements.

In WIV energy harvesting experiments, the blockage rate of the model is a crucial parameter, representing the ratio of the model's cross-sectional area relative to the cross-sectional area of the test channel. A high blockage rate can lead to airflow distortion, thereby compromising the accuracy of experimental results. The blocking rate (β) is calculated using the following equation (Sun et al., 2021):

$$\beta = \frac{A_i}{A_t} \times 100\% \tag{1}$$

where A_i represents the projection area of the IPEH perpendicular to the incoming flow, and A_t denotes the circular cross-sectional area of the test channel. Based on the calculations, the blocking rate of IPEH ranged from 0.059% to 1.005%, which was well below the critical threshold of 5% required to prevent flow obstruction, indicating the reliability of the test bench.

2.2 Experimental model

2.2.1 Test subject

The integrated double-bluff body model proposed in this study, shown in Figure 2(a), comprises an interference column (fixed column), response column, cantilever beam, and piezoelectric material. The interference column is posi-

tioned upstream, while the response column is placed downstream. The passage of the fluid flow through the interference column generates a wake in the area behind it. The wake interaction on the surface of the response column induces substantial vibration, which, in turn, forces cantilever beam deformation. This deformation of the cantilever beam leads to the deformation of the piezoelectric material, generating an electrical signal. In this way, the integrated double-bluff body energy harvester converts fluid kinetic energy into electrical energy under WIV. Compared to existing double-bluff body WIV devices (Du et al., 2024), this integrated layout eliminates the need for external support structures, simplifying the design and enabling easier miniaturization. The fixed end functions efficiently, supporting the integration and enhancing overall system performance. Thus, the device can easily adjust the flow direction to select different vibration mechanisms, even when only one end is fixed. In the opposite arrangement, the response column of the double-bluff body device was positioned upstream, as shown in Figure 2(b). As fluid flows over its surface, alternating vortex shedding occurs, inducing an alternating lift force on its surface, resulting in VIV of the response column.

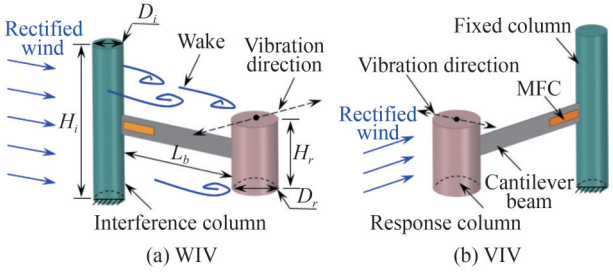


Figure 2 Schematic of the test cases

A wind tunnel experiment was subsequently conducted to examine the factors influencing the performance of the integrated double-bluff body energy harvester. In this experiment, the interference column was fabricated from resin using 3D printing, while the response column was constructed from rigid foam. The two columns were connected by a cantilever beam made of pure aluminum. A piezoelectric material (MFC) was attached to the root of the cantilever beam and connected to an external circuit via wiring. The entire energy-harvesting module was mounted on a fixed base through the interference column and positioned inside a Plexiglas wind tunnel. The structural parameters of the integrated double-bluff body are listed in Table 1.

Additionally, the piezoelectric oscillator was tested in air, neglecting air damping. An impulse force was applied to the response cylinder, and its free-decay vibration was recorded over one second at a sampling rate of 2 000 Hz. The free-decay curves obtained from the experiment and the simulation are presented in Figure 3.

The peak value was substituted into the formula to calculate the damping ratio ζ,

Table 1 Size parameters of integrated double bluff body WIVPEH

Parameter	Value
ρ_b (kg/m^3)	2 700
$S_c/W_c/H_c$ (mm)	13.5/20/0.5
$S_{MFC}/W_{MFC}/H_{MFC}$ (mm)	35/8/0.5
ρ_r (kg/m^3)	34.3
D_r/H_r (mm)	45/70
ρ_i (kg/m^3)	1 150
DBB1: D_i/H_i (mm)	30/160
DBB2: S_i/H_i (mm)	30/160
DBB3: S_i/H_i (mm)	30/160
L_i (mm)	30

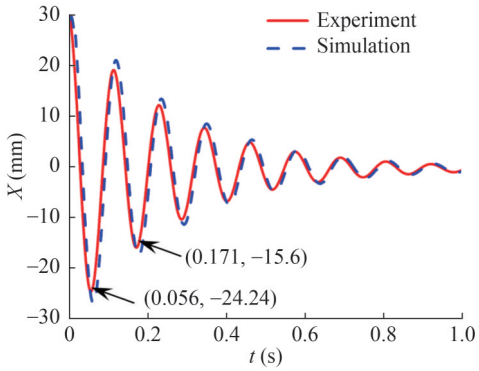


Figure 3 Free vibration attenuation curve

$$\zeta = \frac{1}{2\pi n} \ln\left(\frac{A_n}{A_{n+1}}\right) \tag{2}$$

where A_n denotes the amplitude of the nth cycle. The experiment used $n = 1$. The calculation yielded a damping ratio of 0.07 for the PEH wake oscillator, which was then used in the subsequent two-way FSI simulation.

2.2.2 Cross-sectional shape of interference column

Previous studies have shown that the cross-sectional shape of the interference column plays a crucial role in influencing the vibration and energy-harvesting characteristics of the device (Wang et al., 2023b). In the present study, a new double-bluff body model was developed by altering the cross-sectional shape of the upstream interference column. As shown in Figure 4, these configurations are labeled DBB1, DBB2, and DBB3 from left to right. DBB1, DBB2, and DBB3 corresponded to the double-bluff body arrangements where the cross-sectional shapes of the interference column are circular, square, and triangular, respectively. The fluid flowing through the interference columns with different cross-sectional shapes generates different wake patterns, causing the response column

to exhibit different vibration patterns. A comprehensive set of wind tunnel tests was conducted to explore the effectiveness of these bluff body designs for optimal wind energy harvesting.

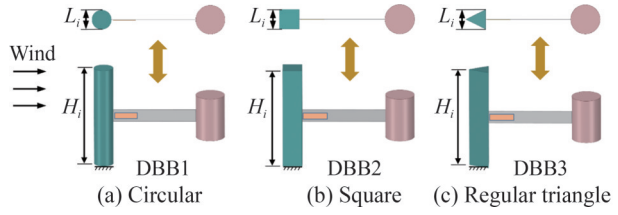


Figure 4 Interference column section model

In the experiment, the stiffness and damping of the cantilever beam structure were kept constant in the VIV and WIV configurations. Additionally, the size of the bluff body used in both excitation mechanisms was identical. When the cross-sectional shape of the interference column was altered, the characteristic length and effective inflow area remained unchanged to ensure consistency across all tests.

2.3 Uncertainty analysis of experimental results

Before the formal experiment, the hot-wire anemometer and the laser displacement sensor were calibrated (Wang et al., 2025). First, an alternating wind speed test was conducted in the channel without the experimental model. The results showed a strong positive linear correlation between wind speed and frequency ($U = 0.382f - 0.35$), which verified the performance of the axial flow fan and the accuracy of the hot-wire anemometer. The laser displacement sensor was then used to measure the structural displacement of the model during the wind tunnel experiment. The experimental results shown in Figure 5 indicated that the output voltage of the sensor increased proportionally with displacement, demonstrating excellent linearity and confirming the reliability of the sensor.

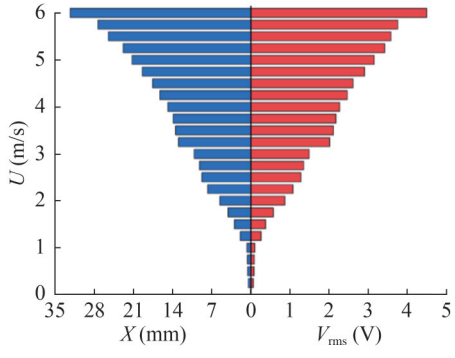


Figure 5 Histogram of laser displacement sensor calibration

To ensure the accuracy of the experimental data, analyzing the uncertainty of the results was crucial. Each test result was derived from the average of 100 data points collected during the experiment. Taking vibration displacement as an example, the standard deviation (S_X) and the uncertainty (E_R) of the experimental results were calculated. The equations used are as follows (Wu et al., 2025):

$$S_X = \sqrt{\frac{1}{n-1}\sum_{i=1}^{n}\left(X_i - X_{\text{avg}}\right)^2} \tag{3}$$

$$E_R = \pm\frac{t_{n-1}S_X}{Y_{\text{avg}}\sqrt{n}} \times 100\% \tag{4}$$

where X_{avg} is the average of the experimental results and t is the confidence factor; for 95% confidence, $t \approx 1.984$. n is the number of tests.

System uncertainty (E_S):

$$E_S = \pm\sqrt{\left(\frac{f_m}{t}\right)^2 + \left(\frac{f_c}{t}\right)^2} \tag{5}$$

Combined uncertainty (E):

$$E = \pm\sqrt{{E_R}^2 + {E_S}^2} \tag{6}$$

where f_m is the measurement error of the data acquisition card, and f_c is the measurement error of the laser displacement sensor.

Taking DBB1 as an example, the uncertainty analysis of the experimental results was conducted, as shown in Table 2. The analysis revealed that, as the wind speed varied, the S_X of the vibration displacement remained below 0.271, while the E_R stayed below 0.004. These values fall within the acceptable range, confirming that the experimental results are highly reliable and accurate.

2.4 CFD setup of PEH

2.4.1 Governing Equations

The interaction between the fluid and the structure in the wake is central to this study. Thus, the fluid control equations were described using the Arbitrary Lagrangian–Eulerian (ALE) coordinates. The continuity equation and Navier–Stokes (N–S) equation in ALE coordinates can be expressed as follows (Zhang et al., 2024):

$$\nabla \cdot (u_f - u_m) = 0 \tag{7}$$

$$\rho_f \frac{\partial u_f}{\partial t} + \rho_f\left(\left(u_f - u_m\right)\cdot\nabla\right) = \nabla\cdot\left(\sigma_f\right) \tag{8}$$

where ρ_f is the fluid density, $u_f$is the fluid velocity, t is the time, and u_m is the grid velocity.

The piezoelectric energy harvesting based on WIV was modeled as a two-way FSI process. In the numerical calculations for two-way FSI, data were exchanged between the fluid and solid domains through the coupling surface

Table 2 Uncertainty analysis of experimental results

v (m/s)	X_{avg} (mm)	S_X	n	DOF (n−1)	t	E_R	f_m	f_c	E_S	E
1	0.728	0.014	100	99	1.984	±0.004	0.0005	0.036	±0.018	±0.0185
2	7.708	0.082	100	99	1.984	±0.002	0.0005	0.036	±0.018	±0.0183
3	12.085	0.152	100	99	1.984	±0.002	0.0005	0.036	±0.018	±0.0183
4	16.288	0.211	100	99	1.984	±0.003	0.0005	0.036	±0.018	±0.0183
5	19.756	0.271	100	99	1.984	±0.003	0.0005	0.036	±0.018	±0.0184

on the device. At this coupling surface, the displacements and velocities of the fluid and solid domains were equal. Within each time step, the fluid and structural equations were solved iteratively, with strict enforcement of displacement and stress continuity at the interface. Forces were transmitted from the fluid domain to the solid domain, and displacements were transmitted from the solid domain to the fluid domain, all through the fluid–solid coupling surface. Aiming to ensure the accuracy of data transmission in the two-way FSI process, the calculation formula for the fluid stress tensor σ_f is as follows (Sarviha and Barati, 2023).

$$\sigma_f = -pI + Mu_f\left[\nabla u_f + \left(\nabla u_f\right)^{\mathrm{T}}\right] \tag{9}$$

In the two-way FSI calculation process described above, the fluid and solid domains must meet boundary condition conservation and force balance conditions on the fluid–solid coupling surface. The formula is presented as follows (Zhang et al., 2025).

$$d_f = d_s, u_f = u_s \tag{10}$$

$$n\sigma_f = n\sigma_s \tag{11}$$

In the coupled solution, the motion equation of the PEH is derived from Hamilton's principle and solved together with the ALE form of the N–Stokes equations (Duan et al., 2022).

$$M_s\ddot{d} + C_s\dot{d} + K_s d = \sigma_f + \sigma_s \tag{12}$$

where M_s, C_s, and K_s are the equivalent mass, equivalent stiffness, and equivalent damping of the solid domain, respectively.

2.4.2 Boundary condition

As illustrated in Figure 6, a three-dimensional computational model of the energy harvester was established.

The computational domain, shown in Figure 6(a), had dimensions of $30D_i \times 10D_i \times 3.1D_i$. The center of the interference column was positioned $5D_i$ away from the left inlet and $25D_i$ away from the right outlet. The left side of the domain was set as a velocity inlet, the right side as a pressure outlet, and the walls were assigned a no-slip boundary condition. To enhance computational efficiency

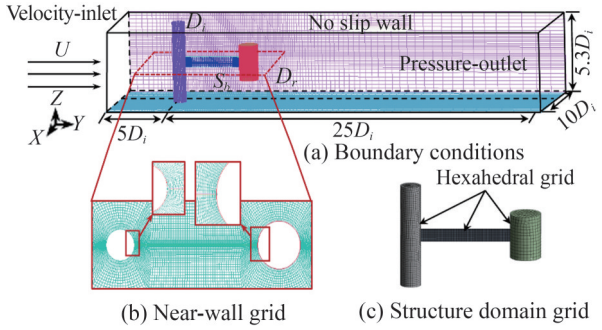


Figure 6 Computational domain and grid division

and accuracy, the fluid domain model was meshed using structured grids. Considering the importance of the near-wall region in fluid dynamics, a boundary layer was added near the model. The first layer height was set at 10^{-4} m, with a growth ratio of 1.2, as shown in Figure 6(b). To ensure a one-to-one correspondence between the nodes of the structure and fluid domains, the structural domain was discretized into a hexahedral grid, as depicted in Figure 6(c).

Owing to the vibration of the model, turbulence emerged in its vicinity. In this study, large eddy simulation (LES) was used as the numerical calculation method, with a dimensionless wall distance of $y^+ = 1$. This value was chosen to provide a balanced resolution across the viscous sublayer, the buffer region, and the near-wall laminar zone (Yao et al., 2025). This value effectively captured small-scale vortical structures near the wall, while preventing excessive grid refinement that would increase computational costs. At the low Reynolds numbers near the onset of WIV, this approach accurately resolved the turbulent structures (Tong et al., 2014). The transient solution was obtained using the Smagorinsky–Lilly sub-grid model with a coefficient Cs = 0.1 (Lysenko et al., 2023). The flow field medium was set as air at room temperature (20 °C). During the discretization process, the finite volume method was applied to discretize the control equations, and the PISO algorithm was used to manage the transient coupling between the pressure and velocity fields. A second-order implicit reverse iteration time-stepping scheme was employed for time integration, and the convection term was discretized using the QUICK scheme. The wall boundary layer was assumed to be fully turbulent and was resolved using LES. The convergence criterion for residual monitoring was set to 10^{-6}, and the time step was determined to be 0.005 s. No divergence or periodic oscilla-

tions were observed during the coupling process, ensuring the stability of the coupled system.

The boundary layer thickness of the bluff body wall substantially influenced vortex shedding and flow-induced forces. When U = 4 m/s, the grid independence verification results of the WIVPEH under different boundary layer thicknesses are shown in Table 3. The results showed that vibration displacement and flow field pressure increased with the boundary layer thickness. The minimum error was 1.46%, and the maximum error was 2.69%. Considering the balance between calculation time and resources, the grid with a boundary layer thickness of 15 was selected for subsequent analysis.

Table 3 Grid independence verification of PEH

Grid	Boundary	X (mm)	Relative error (%)	Pressure (Pa)	Relative error (%)
I	10	13.11	2.69	12.02	2.59
II	15	12.95	1.79	12.16	1.46
III	20	12.99	0	12.34	0

2.5 Date reduction

The vibration displacement and output voltage under each operating condition were recorded using a data acquisition card. To ensure the accuracy of the experimental results, the displacement and voltage data for each working condition were measured in three separate groups and then processed using the three-time average method (Wang et al., 2025).

$$X_{\text{avg}} = \frac{X_1 + X_2 + X_3}{3} \tag{13}$$

$$V_{\text{avg}} = \frac{V_1 + V_2 + V_3}{3} \tag{14}$$

To reveal the vibration and energy-harvesting characteristics of the system at different frequencies and optimize the design of the energy-harvesting device, a frequency-domain analysis of the collected signal was performed. Assuming a time-domain signal $a(n)$ with N sampling points, where n = 0, 1, 2, ⋯, $N-1$, the Fast Fourier Transform (FFT) equation was applied (Al-Alweet et al., 2025).

$$A(k) = \sum_{n=0}^{N-1} a(n) \cdot \mathrm{e}^{-\frac{2\pi \mathrm{i}}{N} kn}, k = 0, 1, 2, \cdots, N-1 \tag{15}$$

where $A(k)$ is the amplitude of the signal at frequency f_k, e is the base of the natural logarithm, and i is an imaginary unit.

The frequency f_k could then be calculated using Eq. (15).

$$f_k = \frac{k}{T} \tag{16}$$

where k is the frequency-domain serial number, and T is the total time of the signal.

The collected vibration and electrical signals are input into Eqs. (14) and (15), leading to the derivation of Eqs. (16) and (17).

$$A_x(f) = \mathrm{FFT}\{X(t)\} \tag{17}$$

$$A_v(f) = \mathrm{FFT}\{V(t)\} \tag{18}$$

where $A_x(f)$ is the vibration amplitude, $A_v(f)$ is the voltage amplitude, $X(t)$ is the vibration displacement at time t, and $V(t)$ is the output voltage at time t.

To accurately evaluate the performance of the system, the root mean square (RMS) value of the vibration displacement of the response column under different working conditions was used to assess the vibration characteristics, while the RMS value of the output power of the energy-harvesting module was used to evaluate the energy-harvesting characteristics. Therefore, the RMS value of the output power is defined as P_{rms}, calculated using the following equation (Wang et al., 2025).

$$P_{\text{rms}} = \frac{V_{\text{rms}}^2}{R} \tag{19}$$

where V_{rms} is the RMS value of the output voltage of the energy harvester, and R is the external resistance. V_{rms} can be calculated using the following equation (Siriyothai and Kittichaikarn, 2023).

$$V_{\text{rms}} = \sqrt{\frac{1}{T}\int_0^T V(t)^2 \mathrm{d}t} \tag{20}$$

Correspondingly, the RMS value X_{rms} of the vibration displacement of the response column was calculated using Eq. (20).

$$X_{\text{rms}} = \sqrt{\frac{1}{T}\int_0^T X(t)^2 \mathrm{d}t} \tag{21}$$

The energy-harvesting module experiences lateral vibration displacement under the action of FIV, with the corresponding force applied to the piezoelectric fiber material through the cantilever beam, facilitating the conversion of fluid kinetic energy into electric energy. Therefore, to analyze the impact of different vibration modes of the double-bluff body model and the cross-sectional shape of the upstream interference column on the kinetic energy-harvesting performance of the fluid in the energy-harvesting module, the relative increase in the multiple P_m of the RMS value of the output power is introduced (Wang et al., 2025).

$$P_m = \frac{P_{\max} - P_{\min}}{P_{\min}} \tag{22}$$

where $P_{\max}$ is the RMS value of the larger output power under different configurations of the double-bluff bodies, and $P_{\min}$ is the smaller RMS value.

In the WIV piezoelectric energy-harvesting process, the fluid kinetic energy input power P_f is defined as follows (Farsi et al., 2021):

$$P_f = \frac{1}{2}\rho_f U^3 H_r\left(D_r + 2X_{\max}\right) \tag{23}$$

where $X_{\max}$ is the maximum displacement of the response column, and $H_r(D_r + 2X_{\max})$ is the projection area of the oscillation interval of the response column. The energy conversion efficiency is calculated using the following equation (Ding et al., 2015):

$$\eta = \frac{P_{\text{rms}}}{P_f} \times 100\% \tag{24}$$

3 Results and discussion

Considering the typical offshore wind speeds and aiming to avoid the vibration effect caused by excessive fan speed, the low wind speed range of 0–6 m/s was selected to examine the vibration displacement, output voltage power, and energy conversion efficiency of the PEH under different cross-sectional shapes (Liu et al., 2025).

3.1 Numerical method validation

After conducting an uncertainty analysis to confirm the experimental accuracy, the numerical results were compared with the experimental data, as shown in Figure 7. The vibration displacement of DBB1 increased with wind speed, reaching its maximum value at U = 6 m/s, where the relative error between the simulation and experimental results was 3.9%. The maximum relative error of 4.9% occurred at U = 4 m/s. These errors remained within the acceptable range reported for similar structural vibration studies (Wu et al., 2021), indicating that the numerical method accurately captured the system vibration characteristics. This verification process also confirmed the validity of neglecting geometric nonlinearity under the current operating conditions.

3.2 Optimal configuration selection

3.2.1 Comparison between WIV and VIV

The curves of vibration displacement and output voltage of the PEH in terms of wind speed under different vibration modes are shown in Figure 8. Vibration displacement and output voltage under VIV initially increased and then decreased as the wind speed increased, displaying a noticeable "lock-in region" that restricted the effective operating range. In this "lock-in region," the vortex shedding frequency of the PEH closely matched the natural frequency of the structure, which remained around 7 Hz. The simulation data showed that the vibration response of the PEH was mainly governed by the first-order bending mode. Referring to Figures 8(a) and (b), when the wind speed ranged from 2.2 m/s to 3 m/s, the vibration displacement and output voltage of the PEH under VIV were temporarily higher than those under WIV. However, at a wind speed of

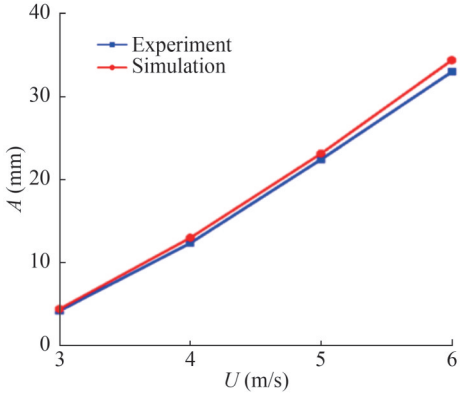


Figure 7 Comparison of DBB1 experiment and simulation displacement results

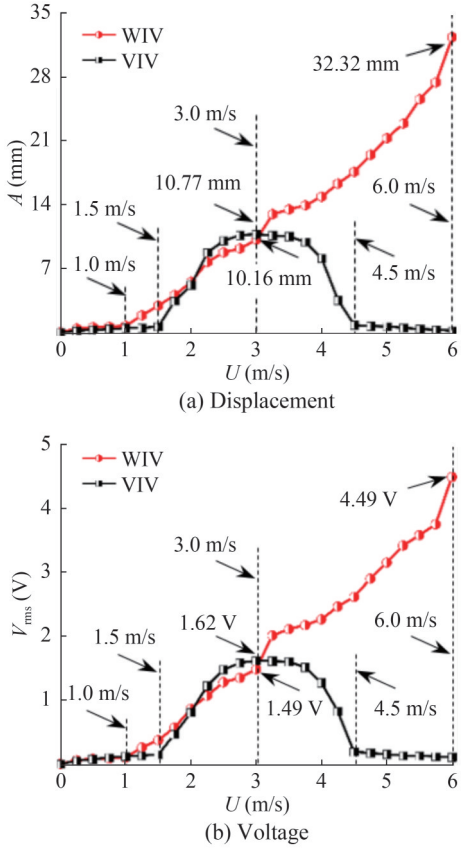


Figure 8 Vibration displacement and output voltage of WIV and VIV with the change of wind speed

3 m/s, the peak values under VIV were only 6% and 8.7% higher than those under WIV, respectively, indicating that the performance improvement was modest. Consistent with previous research, the wake VIV and wake galloping occurred successively in the PEH within the 0–6 m/s wind speed range.

At a wind speed of 3.25 m/s (Re = 6 600), the system reached the wake galloping threshold. Simultaneously, the periodic vortex shedding frequency from the interference cylinder aligned with the first-mode natural frequency of the structure. When Re exceeded 6 600 (U > 3.25 m/s), the system continued to be dominated by the first bending mode, with no mode splitting or activation of higher bending modes. This phenomenon was due to the fact that the equivalent stiffness of the aluminum cantilever beam was matched to the mass of the response cylinder, which caused the natural frequencies to concentrate near the first mode. Finite element analysis predicted the second bending mode at approximately 49 Hz, which was well above the maximum vortex shedding frequency (≤10 Hz) within the test range. The stable, periodic wake excitation provided by the interference cylinder focused its energy on the first mode and lacked the broadband or impulsive components necessary to excite higher modes.

Additionally, the free-decay test shown in Figure 3 produced a decay curve with a single dominant frequency and no beating. The FFT results confirmed that the energy was confined to the first bending mode band. The first-mode frequency calculated by finite element analysis was 8.6 Hz, which differed from the experimental FFT peak of 8.789 Hz by less than 2%, further confirming the dominance of the first mode. Under these conditions, the vibration displacement of the cantilever and the output voltage of the PEH increased rapidly (Wang et al., 2025). When compared to VIV, under WIV, the displacement increased by 200.1%, the output voltage rose by 177.2%, and the effective operating range expanded by 66.7%, notably enhancing the energy-harvesting capability.

To objectively compare the output performance of the integrated double-bluff body piezoelectric energy harvester under WIV and VIV, the study employed qualitative and quantitative analyses. The qualitative analysis was conducted through an LED brightness experiment, as shown in Figure 9.

The real-time vibration state of the double-bluff body model and the real-time brightness of the external circuit LED were depicted from top to bottom under a wind speed of 5.75 m/s. Figures 9(a) and (c) show the experimental phenomena under VIV, while Figures 9(b) and (d) show the experimental phenomena under WIV. Notably, the vibration displacement of the model under VIV was substantially smaller than that under WIV. During this time, the LED remained off. In contrast, the LED emitted steady light under WIV. From a qualitative perspective, this observation indicates that the output performance of the PEH was better under WIV.

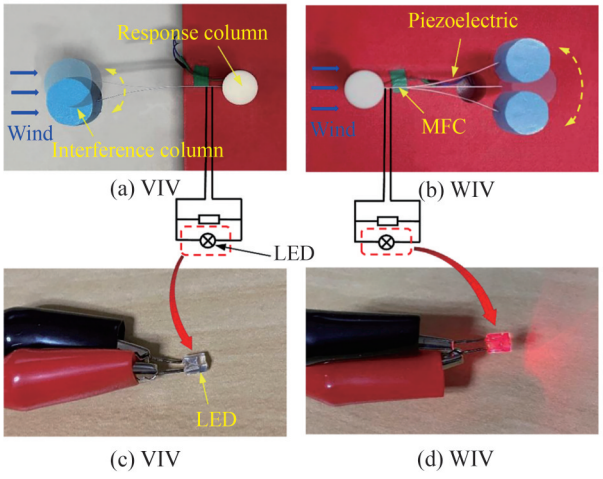


Figure 9 Luminance comparison of LED under WIV and VIV

The quantitative analysis of the voltage signals in the LED brightness experiment is shown in Figure 10. Notably, the output voltage of the PEH under both vibration mechanisms stabilized after 22 s, confirming the feasibility of the integrated double-bluff body model for piezoelectric energy harvesting. Compared to the output voltage of 0.4 V under VIV, the output voltage under WIV reached 6.4 V, a remarkable increase of 15 times. This remarkable enhancement was due to the presence of the interference column, which increased the fluid excitation force in the wake. Consequently, this phenomenon increased the vibration displacement of the response column, generating a higher voltage output (Liu et al., 2020).

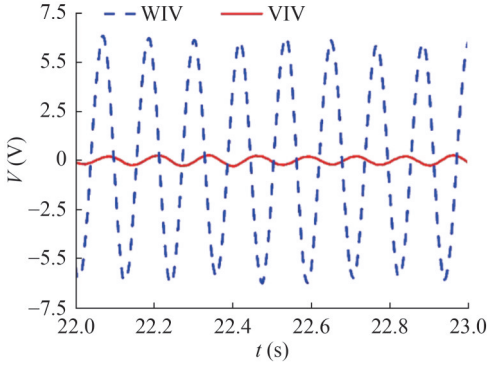


Figure 10 Output voltage variation of the energy-harvesting module under WIV and VIV

Aiming to comprehensively evaluate the energy output in the LED brightness experiment, Figure 11 presents the power output data of the PEH under VIV and WIV. Under VIV, the power output of the PEH was only 0.017 μW, which was insufficient to reach the LED's rated power of 0.028 μW, resulting in an unlit bulb. In contrast, under

WIV, the output power of the PEH reached 14.048 μW, which was 823.5 times higher than under VIV, demonstrating a notably better output performance.

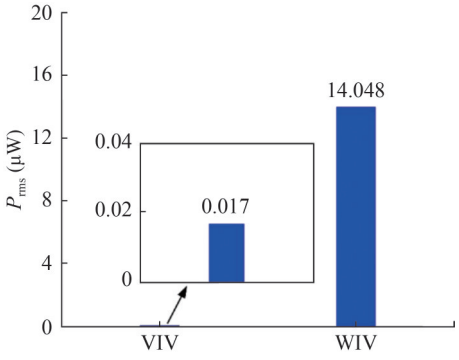


Figure 11 Comparison of energy-harvesting characteristics of PEH in WIV and VIV

Regarding the electrical signal output, the working mechanism of the PEH is elucidated from the perspectives of vibration displacement and flow field, as shown in Figure 12. From Figure 12(a), the PEH underwent single-period motion under VIV and WIV. The vibration displacement under WIV was 29.364 mm, which was 3.6 times higher than that under VIV (6.403 mm), correlating with a higher output voltage and power. This substantial difference in performance can be explained from the flow field perspective, as shown in Figure 12(b). Under WIV, the response cylinder experienced not only the direct impact of the oncoming flow but also the interaction of unsteady vortex structures in the wake of the interference cylinder. This cylinder provided additional energy input for the vibration of the response cylinder, further enhancing its vibration response (Assi et al., 2013). In contrast, under VIV, the vortex shedding generated by the PEH was relatively weak. Consequently, the velocity gradient was not as pronounced and was mainly concentrated around the sides of the cantilever, extending downstream toward the fixed end. This weaker interaction limited the vibration displacement and the energy output. Therefore, the flow under VIV was unable to induce sufficient deformation of the piezoelectric material to generate electrical signals. In contrast, the interference cylinder enhanced the velocity gradient on both sides of the cantilever. The shed vortices rapidly traveled downstream along the cantilever, impacting the surface of the response cylinder and creating localized high-pressure areas. This phenomenon ultimately generated a substantial pressure difference along the vibration direction of the response cylinder, which amplified its vibration response and facilitated a higher electrical output.

The FFT analysis of the vibration displacement and output voltage of the PEH under VIV and WIV is shown in Figure 13, illustrating the correlation between the two. As shown in Figure 13(a), the dominant vibration frequencies of the PEH were 7.813 Hz under VIW and 8.789 Hz under WIV, with the latter being slightly higher. This finding indicates that under WIV, the response cylinder had a shorter vibration period of the response cylinder was and the response and a more intense response, which is consistent with the analysis results shown in Figure 12. Figure 13(b) further confirms that the dominant frequencies for vibration displacement and output voltage were identical, appearing as a single prominent peak without notable harmonics or subharmonics. This observation confirms that, in the corresponding dominant mode, the stable periodic vibration of the response cylinder was effectively converted into electrical energy via the piezoelectric material (Dong et al., 2019), supporting the working mechanism described in Figure 12(b).

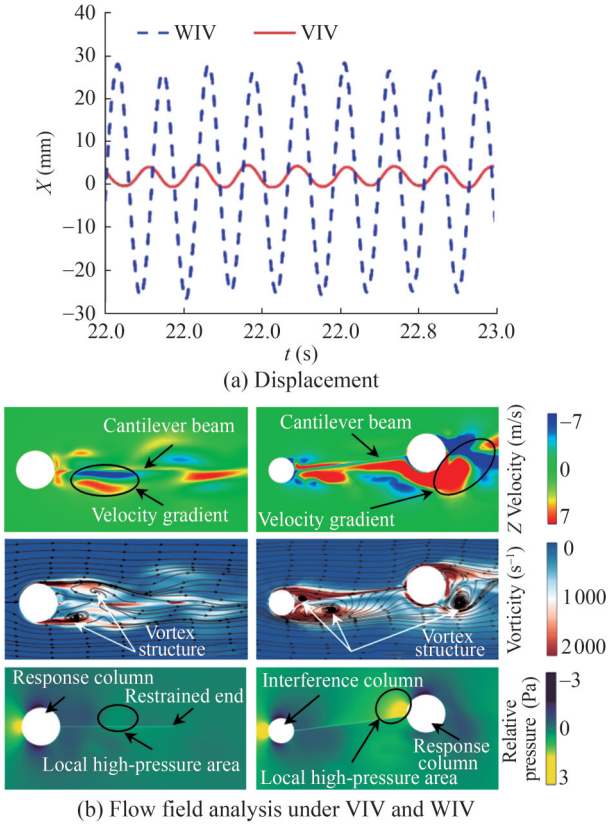


Figure 12 Vibration displacement variation at the cantilever beam end under WIV and VIV

The study highlighted that during the design phase of the cantilever PEH, the addition of an upstream interference column effectively improved the overall output performance of the energy harvester. When compared to the VIV of a single cylindrical device, the WIV mechanism not only increased the amplitude but also the vibration frequency of the response column. Consequently, the output power of the energy harvester under WIV was considerably higher than that under VIV (Wang et al., 2020d).

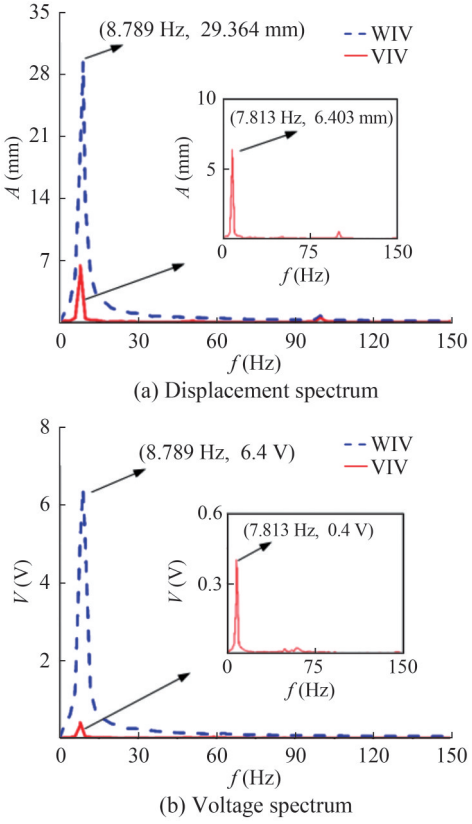


Figure 13 FFT diagram of the energy harvester oscillator under WIV and VIV

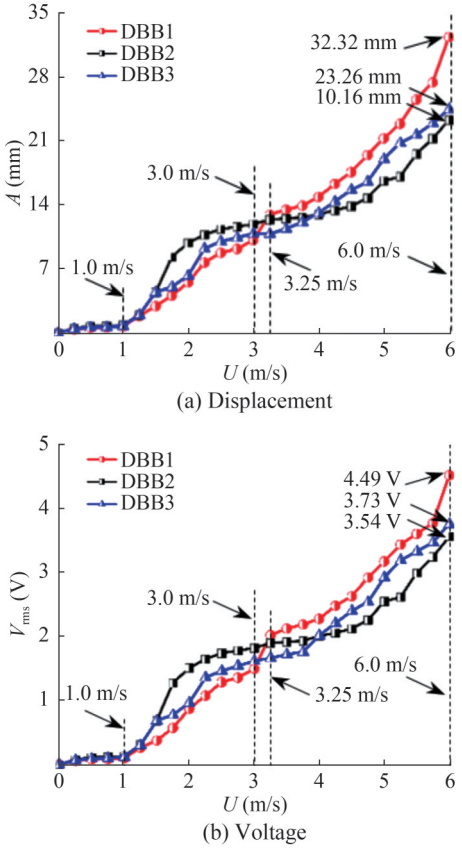


Figure 14 Vibration displacement and output voltage of DBB1–DBB3 with the change of wind speed

3.2.2 Comparison between DBB1–DBB3

By modifying the cross-sectional shape of the interference column, the study further explored the vibration response and output performance of the PEH under WIV. Figure 14 illustrates the relationship between vibration displacement and output voltage for DBB1–DBB3 as a function of wind speed. As wind speed increased, displacement and voltage also showed an upward trend. In Figure 14(a), the vibration displacement of the PEH with different cross-sectional shapes alternately increased with wind speed. Specifically, the displacement of DBB1 gradually surpassed that of DBB2 and DBB3 between 3–3.25 m/s and continued to rise with increasing speed, reaching a peak at 6 m/s. Figure 14(b) shows that the output voltage followed a similar trend to the vibration displacement. After 3.25 m/s, DBB1 exhibited superior output performance. At 6 m/s, the output voltage of DBB1 was 26.84% and 20.38% higher than that of DBB2 and DBB3, respectively. Notably, when the $Re > 6\,600$, the vibration displacement and output voltage of DBB1 consistently outperformed those of DBB2 and DBB3.

Aiming to effectively understand how the cross-sectional shape of the interference column affects the energy-harvesting characteristics under WIV, the vibration response under wake excitation was analyzed. Figure 15 shows the variation in vibration displacement of the response column under WIV at a wind speed of 5.75 m/s for the DBB1–DBB3 models. The vibration behavior of all three models under WIV stabilized, showing a single-cycle motion. Although the fluid flow interacting with the bluff body, having different cross-sectional shapes, impacted the vibration of the downstream response column, the vibration period remained nearly constant. The variations in the shapes of the interference column notably altered the vortex shedding modes behind the bluff body. A stronger vortex shedding mode resulted in a more complex vortex structure, which induced periodic pressure fluctuations in the wake, thereby intensifying the vibration response of the bluff body (Ding et al., 2015). The vibration displacements for DBB1, DBB2, and DBB3 were measured at 29.364, 21.233, and 22.892 mm, respectively. When compared to DBB2 and DBB3, the vibration displacement of DBB1 increased by 38.3% and 28.3%, respectively. Thus, the modification of the cross-sectional shapes of the interference column had a remarkable effect on the vibration characteristics of the models, with DBB1 exhibiting the highest vibration amplitude among the three studied models.

Given that the vibration displacement directly influences the output voltage and power of the PEH, Figure 16 shows the variation in output voltage of the response column when the incoming wind speed was 5.75 m/s. The output voltage from the three different bluff body models remained

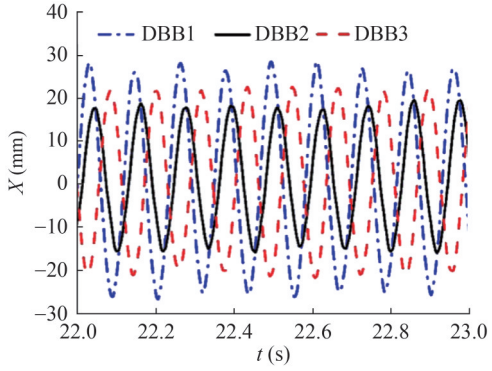


Figure 15 Vibration displacement variations in the response column across the DBB1–DBB3

stable, displaying consistent waveforms throughout the test. Among these models, DBB1 achieved the highest maximum output voltage of 6.4 V, while DBB2 and DBB3 reached output voltages of 4.5 and 5.2 V, respectively. This discrepancy in voltage levels can be attributed to the superior aerodynamic performance and vibration response of the DBB1 model compared to the DBB2 and DBB3 models (Zhu et al., 2019).

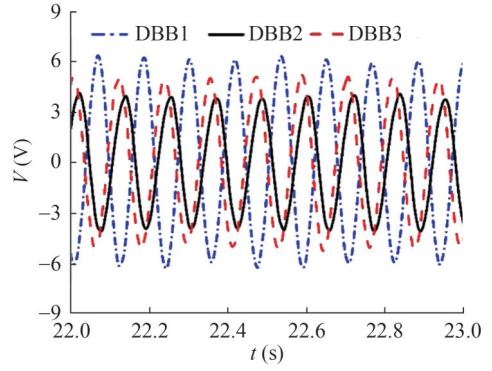
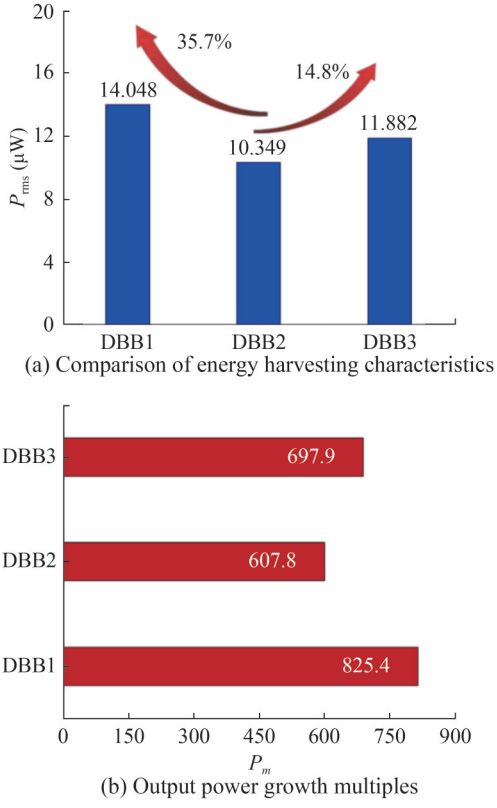


Figure 16 Output voltage variations across the DBB1–DBB3

The changes in vibration displacement and output voltage were clearly synchronized, with both parameters exhibiting similar trends across the different models. A comparison of the output voltage among the three models revealed the following relationships: from DBB2 to DBB3, the vibration displacement increased by 12.4%, which resulted in an 11.7% increase in output voltage. Similarly, from DBB3 to DBB1, the vibration displacement increased by 16.9%, corresponding to a 14.6% increase in output voltage. Despite the different wake excitation effects produced by DBB1–DBB3, a larger vibration displacement consistently correlated with a higher output voltage. Specifically, the WIV caused by the DBB1 model at a specific flow rate resulted in a stronger vibration response compared to that of the DBB2 and DBB3 models.

Based on the output voltage data of the DBB1–DBB3 models shown in Figure 16, the comparison of output performance is illustrated in Figure 17. Figure 17(a) presents a comparison of the energy-harvesting characteristics among DBB1, DBB2, and DBB3. The P_{rms} of the DBB1 model was 14.048 μW, which was 18.2% and 35.7% higher than that of the DBB3 and DBB2 models, respectively. While the energy-harvesting characteristics varied across the DBB1, DBB2, and DBB3 models, all showed improvements when the response column was positioned upstream.

Aiming to compare the energy-harvesting characteristics of the DBB1–DBB3 models, the output power growth relative to that of a single cylindrical bluff body was calculated and defined as P_m, as shown in Figure 17(b). Evidently, the energy-harvesting characteristics of DBB1 increased by a factor of 825.4, while those of DBB2 and DBB3 increased by factors of 607.8 and 697.9, respectively. This enhancement is attributed to the upstream interference column, which effectively improves the energy-harvesting characteristics of the device. By altering the shape of the interference column, higher energy output can be achieved under the same operating conditions (Wang et al., 2023a).



(a) Comparison of energy harvesting characteristics

(b) Output power growth multiples

Figure 17 Comparison of output performance among the DBB1–DBB3

Based on the research results, DBB1 demonstrated higher energy output than the DBB2 and DBB3 models, with increases of 35.7% and 18.2%, respectively. Therefore, DBB1 was identified as having the best energy-harvesting performance and was chosen as the optimal model for this

study. Additionally, the analysis results confirmed the substantial impact of the interference bluff body shape on the vibration and energy-harvesting performance of the device.

3.3 Flow Field Evolution

In this experiment, the displacement amplitude represents the bending degree of the piezoelectric cantilever beam. A large displacement amplitude corresponds to a large bending deformation of the cantilever beam, resulting in a high output voltage. Aiming to explain this phenomenon comprehensively, an analysis from the perspective of the flow field is required. Therefore, four typical velocities were selected to demonstrate the synergistic effect of the vortex shedding process on energy collection performance, as shown in Figure 18.

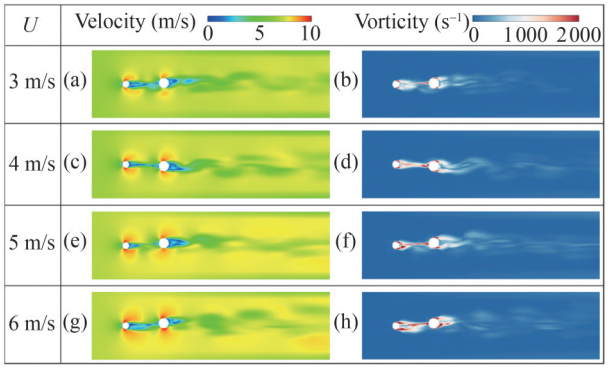


Figure 18 Velocity contours (left) and Vorticity contours (right) in (a–b) 3 m/s, (c–d) 4 m/s, (e–f) 5 m/s, and (g–h) 6 m/s

Notably, the presence of the cantilever beam caused shedding of vortices from the interference cylinder to generate velocity gradients on both sides of the beam. These velocity gradients became more pronounced as the flow velocity increased, thereby inducing substantial vibration in the downstream response cylinder. When the flow velocity was relatively low, the influence range of the interference cylinder's wake was relatively small, and the vortex shedding phenomenon weakened noticeably as the downstream distance increased. However, as the flow velocity increased, the vorticity flux in the wake also increased. With higher vorticity, the vortex shedding became faster, resulting in an enhanced excitation force generated by the fluid on both sides of the response cylinder, which causes a larger vibration displacement (Wang et al., 2025). Therefore, the greater the vorticity flux on both sides of the response cylinder, the larger the vibration displacement and, consequently, the higher the output voltage, as shown in Table 4. Specifically, when the flow velocity was 3 m/s, the vorticity flux on both sides of the response cylinder was 0.07 m²/s, the vibration displacement was 12.1 mm, and the system output voltage was 1.49 V. As the flow velocity increased to 6 m/s, the vorticity flux increased by

Table 4 Effect of flow velocity on PEH performance metrics

U (m/s)	Vorticity flux (m²/s)	X (mm)	V (V)	f_s (Hz)	f_v (Hz)	St
3	0.07	12.11	1.49	7.30	8.20	0.1100
4	0.18	14.53	2.26	7.90	8.48	0.0900
5	0.39	21.32	3.15	8.62	8.73	0.0776
6	0.86	32.32	4.49	8.90	8.80	0.0700

11.29 times, the vibration displacement increased by 2.67 times, and the output voltage increased by 2.01 times. Notably, as the vorticity flux increased, the vibration displacement of the response cylinder also substantially increased, thereby enhancing the output voltage of the PEH (Du et al., 2024).

The qualitative analysis shown in Figure 18 and the quantitative data listed in Table 4 revealed that, as the flow velocity increased, the vortex shedding frequency (f_s) gradually synchronized with the vibration frequency (f_v) of the wake oscillator. Within this synchronized range, the Strouhal number stabilized between 0.07 and 0.11, corresponding to the locked-in regime induced by vortex shedding, with no clear vortex merging observed. Although the cantilever beam disturbed the wake and prevented the formation of the typical 2S or 2P pattern, the vortices continued to detach in a periodic alternating sequence. This periodicity was clearly indicated by the stable Strouhal number. The observed Strouhal range matched the characteristic values reported in (Wang et al., 2020b) for cantilevered structures undergoing periodic VIV. Consequently, even though the 2S or 2P pattern did not appear, the periodic features of the atypical vortex structure could still be classified and identified through this stable Strouhal range. From the perspective of the flow field, this analysis is consistent with the pattern shown in Figure 14 and further clarifies the working mechanism of the PEH under WIV as the flow velocity changes.

3.4 Performance analysis of PEH

As the wind velocity changes, the complex flow field environment notably affects the vibration characteristics of the response column, thereby affecting the output performance of the device. Aiming to comprehensively evaluate the output performance of the device in practical applications, Figure 19 illustrates the relationship between output power and energy conversion efficiency for DBB1–DBB3 across different wind speeds.

As shown in Figure 19(a), the output power of DBB1–DBB3 increased with rising velocity. This trend was attributed to the higher maximum oscillating lift that the response column could withstand as the wind speed increased, leading to greater power output (Yan et al., 2021). Over the range of low to medium wind speeds, the output

power of the three devices fluctuated alternately. Between 3 and 3.25 m/s, the output power of DBB1 successively exceeded that of DBB3 and DBB2. Once the wind speed exceeded 3.25 m/s, the output power of DBB1 stabilized at a high level. At a wind speed of 4 m/s, the output power of DBB3 surpassed that of DBB2. Notably, at wind speeds below 4 m/s, the advantageous output power intervals for the three devices were relatively short, making it difficult to accurately assess their output performance. However, as the wind speed increased, the relationship between the output power of the devices became relatively stable. At a wind speed of 6 m/s, the output power of all three devices reached their respective maxima. At this point, the output power of DBB1 was 20.13 μW, which was 60.65% and 44.4% higher than that of DBB2 and DBB3, respectively.

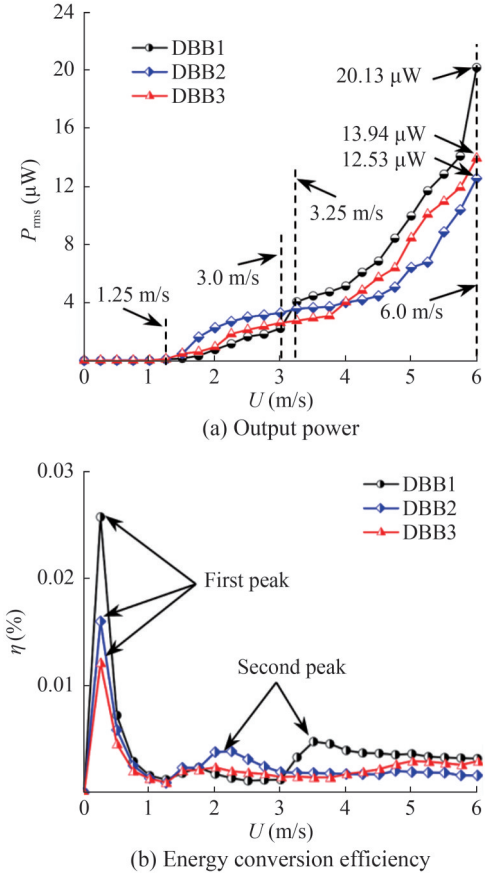


Figure 19 Output power and energy conversion efficiency

Equations (19)–(24) show that the energy conversion efficiency of the PEH is directly proportional to the square of the output voltage and inversely proportional to the cube of the wind speed. As wind speed increased, the fluid kinetic power input also increased with the cube of the velocity ($P_f \propto U^3$), while the electrical output power grew with the square of the wind speed ($P_{rms} \propto V_{rms}^2 \propto U^2$). The disparity between these growth rates resulted in an initial rise in conversion efficiency, followed by a rapid decline at higher speeds, as shown in Figure 19(b). The first peak in energy conversion efficiency occurred at 0.25 m/s. Although this was not yet the critical wind speed for WIV, the difference in size between the response cylinder and the interference cylinder caused the downstream response cylinder to operate under its own VIV. However, after this first peak, it quickly disappeared, failing to provide stable energy output for the micro-sensor. As wind speed continued to increase, DBB2 and DBB1 successively reached their respective second peaks. Notably, the second peak of DBB1 was 23.4% higher than that of DBB2, and its coverage area was 2.4 times larger, enabling DBB1 to maintain a more stable energy output over a broader range of wind speeds.

4 Conclusions

In this study, an integrated double-bluff body PEH was introduced to enhance energy harvesting using WIV. The output performance of the PEH was evaluated under different vibration modes and cross-sectional shapes of the interference column through wind tunnel experiments. Additionally, the working mechanism of the PEH was explained based on two-way fluid–structure interaction theory. The following conclusions were drawn:

1) The output performance of the PEH under WIV was significantly improved. Compared to VIV, the maximum vibration displacement of the PEH under WIV increased by 200.1%, the maximum output voltage increased by 177.2%, and the effective working range expanded by 66.7%.

2) When the interference column had a circular cross-section, the PEH exhibited the best performance under WIV. Compared to square and equilateral triangular cross-sections, the maximum output power of the PEH with a circular cross-section increased by 60.65% and 44.4%, respectively.

3) The evolution of the flow field demonstrated that the energy-harvesting characteristics of the device were sensitive to variations in the incident wind speed. As the wind speed gradually increased, the vibration displacement and output power of the integrated double-bluff body model increased rapidly.

4) When the cross-section of the interference column was circular, the energy output of the PEH became highly stable. Compared to the square cross-section, the energy conversion efficiency at the second peak increased by 23.4% for the circular cross-section. Additionally, the peak coverage range expanded by 2.4 times, allowing stable energy output across a wider operating range.

This study investigated the piezoelectric energy harvesting under low wind speed conditions ranging from 0 to 6 m/s. The results confirmed the energy harvesting advantages of

the DBB1 structure. Future work aims to enhance the test setup to extend the wind speed range and incorporate nonlinear beam theory to improve model accuracy under large displacement conditions. Additionally, the energy conversion process will be further analyzed to examine the impact of mechanical–electrical phase characteristics and impedance matching on conversion efficiency. Machine learning techniques are also planned to optimize the piezoelectric thickness and resonator topology for better performance in complex settings (Jalali et al., 2024).

Funding Supported by the National Natural Science Foundation of China (No. 51905211), a Project of the "20 Regulations for New Universities" funding program of Jinan (No. 202228116), and the Natural Science Foundation of Shandong Province (No. ZR2020ME137).

Competing interests The authors have no competing interests to declare that are relevant to the content of this article.

References

Abdelkefi A, Hajj MR, Nayfeh AH (2012) Piezoelectric energy harvesting from transverse galloping of bluff bodies. Smart Materials and Structures 22(1): 015014. http://dx. doi.org/10.1088/0964-1726/22/1/015014

Al-Alweet FM, Almutairi Z, Alothman OY, Peng Z, Alshammari BA, Almakhlafi A (2025) Time-dependent analysis of flow pattern developments in two-phase flow using capacitance sensors: Fast fourier transform and total power spectrum exploration. Flow Measurement and Instrumentation 102: 102818. https://doi.org/10.1016/j.flowmeasinst.2025.102818

Assi GDS, Bearman PW, Carmo BS, Meneghini JR, Sherwin SJ, Willden RHJ (2013) The role of wake stiffness on the wake-induced vibration of the downstream cylinder of a tandem pair. Journal of Fluid Mechanics 718: 210-245. https://doi.org/10.1017/jfm.2012.606

Ding L, Zhang L, Wu C, Mao X, Jiang D (2015) Flow induced motion and energy harvesting of bluff bodies with different cross sections. Energy Conversion and Management 91: 416-426. https://doi.org/10.1016/j.enconman.2014.12.039

Dong L, Closson AB, Jin C, Trase I, Chen Z, Zhang JX (2019) Vibration-energy-harvesting system: transduction mechanisms, frequency tuning techniques, and biomechanical applications. Advanced Materials Technologies 4(10): 1900177. https://doi.org/10.1002/admt.201900177

Du X, Chen H, Li C, Li Z, Wang W, Guo D, Yu H, Wang J, Tang L (2024) Wake galloping piezoelectric-electromagnetic hybrid ocean wave energy harvesting with oscillating water column. Applied Energy 353: 122081. https://doi.org/10.1016/j.apenergy.2023.122081

Duan D, Cheng Y, Ge M, Bi W, Ge P, Yang X (2022) Experimental and numerical study on heat transfer enhancement by flow-induced vibration in pulsating flow. Applied Thermal Engineering 207: 118171. https://doi.org/10.1016/j.applthermaleng.2022.118171

Eugeni M, Elahi H, Fune F, Lampani L, Mastroddi F, Romano GP, Gaudenzi P (2020) Numerical and experimental investigation of piezoelectric energy harvester based on flag-flutter. Aerospace Science and Technology 97: 105634. https://doi. org/10.3390/mi11100933

Farsi M, Shariatzadeh MJ, Bijarchi MA, Pournasiri Masouleh E, Shafii MB (2021) Low-speed wind energy harvesting from a vibrating cylinder and an obstacle cylinder by flow-induced vibration effect. International Journal of Environmental Science and Technology 19: 1261-1272. https://doi.org/10.1007/s13762-021-03241-1

Franzini GR, Bunzel LO (2018) A numerical investigation on piezoelectric energy harvesting from vortex-induced vibrations with one and two degrees of freedom. Journal of Fluids and Structures 77: 196-212. https://doi.org/10.1016/j.jfluidstructs.2017.12.007

Hu G, Liu F, Li L, Li C, Xiao Y, Kwok KCS (2019) Wind energy harvesting performance of tandem circular cylinders with triangular protrusions. Journal of Fluids and Structures 91: 102780. https://doi.org/10.1016/j.jfluidstructs.2019.102780

Jalali S, Baniadam M, Maghrebi M (2024) Impedance value prediction of carbon nanotube/polystyrene nanocomposites using tree-based machine learning models and the Taguchi technique. Results in Engineering 24: 103599. https://doi.org/10.1016/j.rineng.2024.103599

Latif U, Younis MY, Idrees S, Uddin E, Abdelkefi A, Munir A, Zhao M (2023) Synergistic analysis of wake effect of two cylinders on energy harvesting characteristics of piezoelectric flag. Renewable and Sustainable Energy Reviews 173: 113114. https://doi.org/10.1016/j.rser.2022.113114

Liu FR, Zhang WM, Zhao LC, Zou HX, Tan T, Peng ZK, Meng G (2020) Performance enhancement of wind energy harvester utilizing wake flow induced by double upstream flat-plates. Applied Energy 257: 114034. https://doi.org/10.1016/j.apenergy.2019.114034

Liu S, Zhang L, Lu J, Zhang X, Wang K, Gan Z, Liu X, Jing Z, Cui X, Wang H (2025) Advances in urban wind resource development and wind energy harvesters. Renewable and Sustainable Energy Reviews 207: 114943. https://doi.org/10.1016/j.rser.2024.114943

Lysenko DA, Donskov M, Ertesvag IS (2023) Large-eddy simulations of the flow past a bluff-body with active flow control based on trapped vortex cells at Re = 50 000. Ocean Engineering 280: 114496. https://doi.org/10.1016/j.oceaneng.2023.114496

Sarviha A, Barati E (2023) Piezoelectric energy harvester for scavenging steady internal flow energy: a numerical investigation. Journal of the Brazilian Society of Mechanical Sciences and Engineering 45(8): 398. https://doi.org/10.1007/s40430-023-04338-z

Siriyothai P, Kittichaikarn C (2023) Performance enhancement of a galloping-based energy harvester with different groove depths on square bluff body. Renewable Energy 210: 148-158. https://doi.org/10.1016/j.renene.2023.04.027

Sun W, Liu L, Li Y, Huang C, Chen X, Feng M (2021) Insight into vented explosion mechanism and premixed flame dynamics in linked vessels: Influence of membrane thickness and blocking rate. Journal of Loss Prevention in the Process Industries 72: 104581. https://doi.org/10.1016/j.jlp.2021.104581

Tong B, Wang Y, Yang Q, Su Y, Yi W (2014) Numerical prediction for the hydrodynamic performance of a ferry propeller. Chinese Journal of Ship Research 9(1): 52-58. https://dx.doi.org/10.3969/j.issn.1673-3185.2014.01.008

Wang J, Geng L, Ding L, Zhu H, Yurchenko D (2020a) The state-of-the-art review on energy harvesting from flow-induced vibrations. Applied Energy 267: 114902. https://doi.org/10.1016/j.apenergy.2020.114902

Wang J, Gu S, Zhang C, Hu G, Chen G, Yang K, Li H, Lai Y, Litak G, Yurchenko D (2020b) Hybrid wind energy scavenging by coupling vortex-induced vibrations and galloping. Energy Conversion and Management 213: 112835. https://doi.org/10.1016/j.

enconman.2020.112835

Wang J, Su Z, Li H, Ding L, Zhu H, Gaidai O (2020c) Imposing a wake effect to improve clean marine energy harvesting by flow-induced vibrations. Ocean Engineering 208: 107455. https://doi.org/10.1016/j.oceaneng.2020.107455

Wang J, Sun S, Tang L, Hu G, Liang J (2021) On the use of metasurface for Vortex-Induced vibration suppression or energy harvesting. Energy Conversion and Management 235: 113991. https://doi.org/10.1016/j.enconman.2021.113991

Wang J, Tang L, Zhao L, Zhang Z (2019) Efficiency investigation on energy harvesting from airflows in HVAC system based on galloping of isosceles triangle sectioned bluff bodies. Energy 172: 1066-1078. https://doi.org/10.1016/j.energy.2019.02.002

Wang J, Xia B, Yurchenko D, Litak G, Li Y, Tian H (2023a) Enhanced performance of piezoelectric energy harvester by two asymmetrical splitter plates. Ocean Engineering 270: 113614. https://doi.org/10.1016/j.oceaneng.2022.113614

Wang J, Xia B, Yurchenko D, Tian H (2023b) Enhanced performance of cutting angle cylinder piezoelectric energy harvester via coupling vortex-induced vibration and galloping. Mechanical Systems and Signal Processing 205: 110838. https://doi.org/10.1016/j.ymssp.2023.110838

Wang J, Zhang C, Gu S, Yang K, Li H, Lai Y, Yurchenko D (2020d) Enhancement of low-speed piezoelectric wind energy harvesting by bluff body shapes: Spindle-like and butterfly-like cross-sections. Aerospace Science and Technology 103: 105898. https://doi.org/10.1016/j.ast.2020.105898

Wang J, Zhang C, Hu G, Liu X, Liu H, Zhang Z, Das R (2022) Wake galloping energy harvesting in heat exchange systems under the influence of ash deposition. Energy 253: 124175. https://doi.org/10.1016/j.energy.2022.124175

Wang M, Duan D, Zhang X, Gao C, Yang X, Zhang H (2025) Influence of diameter/aspect ratio on the output performance of wake-induced vibration piezoelectric energy harvester. Physics of Fluids 37(5): 055130. https://doi.org/10.1063/5.0269478

Wu HX, Liao RQ, Qin HN, Zhang XK, Wang D (2025) Low-flow measurement of oil–water two-phase flow based on the dynamic swirling differential pressure method. Physics of Fluids 37(3): 033356. https://doi.org/10.1063/5.0260550

Wu Q, Zhang K, Wang S (2021) Flow and heat transfer characteristics in swirling fluidized bed. China Powder Science and Technology 27(3): 16-24. (in Chinese) https://doi:10.13732/j.issn.1008-5548.2021.03.003

Yan Z, Shi G, Zhou J, Wang L, Zuo L, Tan T (2021) Wind piezoelectric energy harvesting enhanced by elastic-interfered wake-induced vibration. Energy Conversion and Management 249: 114820. https://doi.org/10.1016/j.enconman.2021.114820

Yang K, Su K, Wang J, Wang J, Yin K, Litak G (2020) Piezoelectric wind energy harvesting subjected to the conjunction of vortex-induced vibration and galloping: comprehensive parametric study and optimization. Smart Materials and Structures 29(7): 075035. https://doi.org/10.1088/1361-665X/ab870e

Yao Y, Hu Q, Tang L, Fu T, Shan L, Li T (2025) Effect of curvature and taper on the hydrodynamic properties of seal whisker inspired cylinders in uniform flow and wake. Ocean Engineering 329: 121184. https://doi.org/10.1016/j.oceaneng.2025.121184

Zhang LB, Abdelkefi A, Dai HL, Naseer R, Wang L (2017) Design and experimental analysis of broadband energy harvesting from vortex-induced vibrations. Journal of Sound and Vibration 408: 210-219. https://doi.org/10.1016/j.jsv.2017.07.029

Zhang M, Wang J (2016) Experimental study on piezoelectric energy harvesting from vortex-induced vibrations and wake-induced vibrations. Journal of Sensors 2016: 2673292. https://doi.org/10.1155/2016/2673292

Zhang X, Duan D, Wang M, Gao C, Yang X, Zhang H (2024) Heat transfer enhancement characteristics of multiconfiguration blunt-headed cylinder by flow-induced vibration. Journal of Thermophysics and Heat Transfer 39(3): 1-10. https://doi.org/10.2514/1.T7086

Zhang X, Duan D, Wang M, Gao C, Yang X, Zhang H (2025) Numerical study on vibration heat transfer enhancement of multi-configured blunt-headed cylinder with fin device. International Journal of Thermal Sciences 210: 109573. https://doi.org/10.1016/j.ijthermalsci.2024.109573

Zhao D, Zhou J, Tan T, Yan Z, Sun W, Yin J, Zhang W (2021) Hydrokinetic piezoelectric energy harvesting by wake induced vibration. Energy 220: 119722. https://doi.org/10.1016/j.energy.2020.119722

Zhu H, Tang T, Zhou T, Cai M, Gaidai O, Wang J (2021) High performance energy harvesting from flow-induced vibrations in trapezoidal oscillators. Energy 236: 121484. https://doi.org/10.1016/j.energy.2021.121484

Zhu H, Zhang C, Liu W (2019) Wake-induced vibration of a circular cylinder at a low Reynolds number of 100. Physics of Fluids 31(7): 073606. https://doi.org/10.1063/1.5106407

Zuo W, Li Q, He Z, Li Y (2020) Numerical investigations on thermal performance enhancement of hydrogen-fueled micro planar combustors with injectors for micro-thermophotovoltaic applications. Energy 194: 116904. https://doi.org/10.1016/j.energy.2020.116904